Conversion of Channelrhodopsin into a Light-Gated Chloride Channel

Jonas Wietek,[1]* J. Simon Wiegert,[2]* Nona Adeishvili,[1] Franziska Schneider,[1] Hiroshi Watanabe,[3] Satoshi P. Tsunoda,[1] Arend Vogt,[1] Marcus Elstner,[3] Thomas G. Oertner,[2]† Peter Hegemann[1]†

The field of optogenetics uses channelrhodopsins (ChRs) for light-induced neuronal activation. However, optimized tools for cellular inhibition at moderate light levels are lacking. We found that replacement of E90 in the central gate of ChR with positively charged residues produces chloride-conducting ChRs (ChloCs) with only negligible cation conductance. Molecular dynamics modeling unveiled that a high-affinity Cl^--binding site had been generated near the gate. Stabilizing the open state dramatically increased the operational light sensitivity of expressing cells (slow ChloC). In CA1 pyramidal cells, ChloCs completely inhibited action potentials triggered by depolarizing current injections or synaptic stimulation. Thus, by inverting the charge of the selectivity filter, we have created a class of directly light-gated anion channels that can be used to block neuronal output in a fully reversible fashion.

Channelrhodopsins (ChRs), light-gated ion channels that serve as sensory photoreceptors in microalgae (*1*–*3*), are now widely used to activate specific neuronal populations in the brain. ChR2 and numerous engineered variants have been demonstrated to induce rapid depolarization, reliably triggering single action potentials (APs) in response to brief light pulses. ChRs with extended open-state lifetimes (step-function rhodopsins), on the other hand, provide sustained depolarization and drive AP trains at high frequencies (*4*, *5*). To study the function of specific classes of neurons within large neuronal networks or in the intact brain, transient inactivation by hyperpolarization can be even more informative than depolarization. For this purpose, light-activated ion pumps have been used as membrane hyperpolarizers (*6*, *7*). Because only a single charge is transported per photocycle, these pumps require constant illumination of high intensities. For in vivo experiments, in which photon capture is typically the rate-limiting step, effective inhibition is restricted to a very small volume, even when light-driven pumps with high cycling rates are used (*8*).

As an alternative approach, several attempts have been made to convert ChR into a K^+- or anion-selective channel that might generate outward currents in neurons. However, the preference for K^+ over Na^+ could only be improved by a factor of 2.5, which is not sufficient to create a truly inhibitory tool (*9*, *10*). To convey light-induced neuronal inhibition, we sought to engineer an anion-selective ChR. Electrophysiological data showed that multiple glutamates and lysines are present in transmembrane helix 2 (TM2) of ChR and that these residues line its water-filled pore to transport H^+ and other cations when the channel is open (*11*–*14*). Replacement of these glutamates gradually reduced pore conductance with only small effects on ion selectivity in nearly all cases, with the exception of E90 (*15*). Because of its direct contact with the retinal Schiff base (*9*) and its protonation change during the photocycle, E90 plays a critical role in ion conductance and gating (*12*, *13*, *16*, *17*).

We performed molecular dynamics (MD) simulations (Fig. 1A), taking the x-ray crystal structure of the ChR1/ChR2 hybrid C1C2 as a starting point (*9*, *18*). On the basis of electrical studies on ChR2 wild type and mutants, we assumed that both active side residue E123 and D253 in close proximity to the retinal Schiff base nitrogen are deprotonated (*14*, *19*, *20*). In contrast, the nearby E90 is protonated and forms a hydrogen bond with N258, which forms another hydrogen bond with S63 (fig. S1A). On the basis of MD simulations, we derived structural models for ChR2 and E90 mutants from a most-likely structure (*18*, *21*). For these structural templates, we next computed the water and ion distributions in the protein interior using a reference interaction site model (3D-RISM) (*22*, *23*). The water distribution exhibits a discontinuity around E90 (Fig. 1A), which is in agreement with the water density in the C1C2 x-ray structure (*9*). This finding in combination with recent electrophysiological and spectroscopic results (*9*–*13*, *16*, *17*) suggests that S63, E90, D253, and N258 together with E123 constitute the central gate. This gate acts as a hydrophobic barrier in darkness and prevents water from entering the inner vestibule between the central gate and an inner gate, the latter composed of Y70, E82, E83, H134, and H265 (*9*). After chromophore photoactivation, these barriers undergo substantial conformational changes and convert ChR to a pre-active state. We propose that pre-active ChR requires only minor structural alterations or proton transfer reactions to be capable of opening fully for ion conductance (*16*, *17*, *24*).

To alter ChR ion selectivity, we replaced the central gate E90 with a lysine that we assumed to be protonated under all physiological conditions. This mutation was combined with the T159C substitution to improve membrane targeting of the protein and retinal binding in the chromophore pocket (*25*, *26*). Photocurrents of ChR2-E90K-T159C (C2-EK-TC) in human embryonic kidney (HEK) 293 cells were weak at high extracellular pH (pH_e) (Fig. 2, A and B) but greatly enhanced at low pH_e (Fig. 2C). At low pH_e, both inward- and outward-directed currents were enhanced, and the reversal potential (E_{rev}) shifted only marginally to become more positive (Fig. 2, C and D, and fig. S2, A to C). These results suggest that although activated by protons, the channel did not conduct protons even at low pH_e. Next, we replaced Na^+ (140 mM)

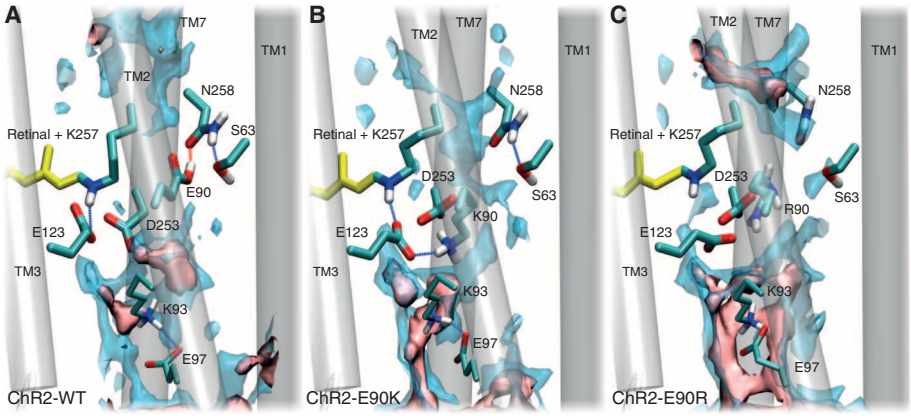

Fig. 1. Structural models obtained from MD simulation. All structures were modeled based on the x-ray crystal structure of the C1C2 chimeric protein (*9*). Water and Cl^- distributions, which are calculated with 3D-RISM, are depicted in light blue and pink, respectively, and the retinal is shown in yellow. (**A**) Model structure of wild-type C2, including the central gate and counterion residues. (**B**) Corresponding model structure of C2-EK. (**C**) Respective C2-ER model structure.

[1]Institute for Biology, Experimental Biophysics, Humboldt Universität zu Berlin, D-10115 Berlin, Germany. [2]Institute for Synaptic Physiology, Center for Molecular Neurobiology Hamburg, Falkenried 94, D-20251 Hamburg, Germany. [3]Institute of Physical Chemistry, Karlsruhe Institute of Technology, Karlstrasse 12, D-76131 Karlsruhe, Germany.

*These authors contributed equally to this work.
†Corresponding author. E-mail: hegemann@rz.hu-berlin.de (P.H.); thomas.oertner@zmnh.uni-hamburg.de (T.G.O)

with K^+, *N*-methyl-glucamine$^+$ (NMG^+), Ca^{2+}, or Mg^{2+} (Fig. 2, C and D, and fig. S2, D to F) and measured the photocurrent conducted by C2-EK-TC. High Ca^{2+} increased photocurrents slightly in both directions; however, none of the cation replacements altered E_{rev}. Thus, external binding of H^+, and to a lower extent Ca^{2+}, enhanced the conductance without transport of the respective cations. Last, we replaced most of the external Cl^- (150 mM) with aspartate$^-$ to produce an extracellular solution with 10 mM Cl^- and 140 mM Asp^-. Under these conditions, currents were inward directed (Fig. 2E), and E_{rev} for both the initial (I_0) and stationary (I_S) currents shifted to +73 mV (Fig. 2, C and D). These data suggested that the observed inward currents were due to an efflux of Cl^- ions.

To investigate subcellular localization, we generated mCherry-tagged ChR-EK derivatives. Partial membrane targeting and considerable cytoplasmic fluorescence (fig. S3) suggested possible folding defects caused by charge repulsion between K90 and K93. To overcome this deficit, we delocalized the charge by replacing E90 with arginine. Photocurrents of ChR2-E90R-T159C (C2-ER-TC) were similar to those of C2-EK-TC, except that improved expression and membrane targeting was observed (fig. S3). In addition, E_{rev} under standard conditions was slightly more negative because of further reduction in H^+ conductance (E_{rev} = −38 mV) (fig. S4, B to D), making this double mutant promising for inhibition of neuronal activity. From this point forward, C2-ER-TC will be referred to as the chloride-conducting ChR (ChloC).

To further characterize the selectivity of C2-EK-TC and ChloC, we measured the photocurrent under variable Cl^- conditions. High symmetrical Cl^- evoked symmetrical currents, and a gradual reduction in external chloride promoted inward-directed currents, with a concomitant shift of E_{rev} to more positive values (Fig. 3A and fig. S3). The presence of only 10 mM chloride on both sides of the membrane resulted in reduced, symmetrical currents in both directions. Stepwise increases in external chloride promoted Cl^- influx, which was observed as outward currents with a shift in E_{rev} to more negative values (Figs. 2F and 3, A to C, and figs. S4 and S5, A to D). The E_{rev} values for I_S were slightly more positive as compared with I_0 owing to transition from open state O1 to O2 with slightly different selectivity profiles (Fig. 3D and figs. S4 and S5) (*27–30*).

To fully exploit the potential of ChloC as a neuronal silencer and to optimize it for low-light conditions, we explored step-function mutants after modification of the DC gate (C128 and D156) (fig. S1). ChR2-E90R-D156N-T159C-expressing cells (slow ChloC) showed the largest photocurrent amplitudes, low inactivation in continuous light or upon repetitive flashing, and a mean open-state lifetime of ~10 s (Fig. 3, C to G). E_{rev} of slow ChloC was even more negative (–54 mV) as compared with that of EK-TC (–27 mV), ChloC (−38 mV) (Fig. 3C and D), and ChR2 wild type (fig. S6). Upon continuous illumination, cells expressing slow ChloC needed almost 10,000 times lower light intensities to produce photocurrents comparable with ChloC at saturation (Fig. 3, H and I).

To better understand the influence of the E90K and E90R mutations, we analyzed extended MD simulations for these mutants, showing that the hydrogen bond to N258 is lost in both cases. In the E90K mutant, the positively charged lysine residue was reoriented toward the active site and formed hydrogen bonds with the counterions (Fig. 1B). In E90R, orientation of the guanidinium group was more flexible (fig. S7, A to C), pointing to E123 in the active site in the predominantly populated conformation seen in Fig. 1C. Furthermore, hydrogen bonding between N258 and S63 was weaker, especially in E90R, leading to greater flexibility as indicated by larger fluctuations in the hydrogen bonding distances (table S1). Because these residues form hydrogen bonds between helices 1 and 7, weaker bonds led to larger displacement of the two helices. As a result, a larger cavity was created at the expense of protein stability. We computed the ion distribution using 3D-RISM, showing a noncontinuous distribution of Cl^- ions in wild

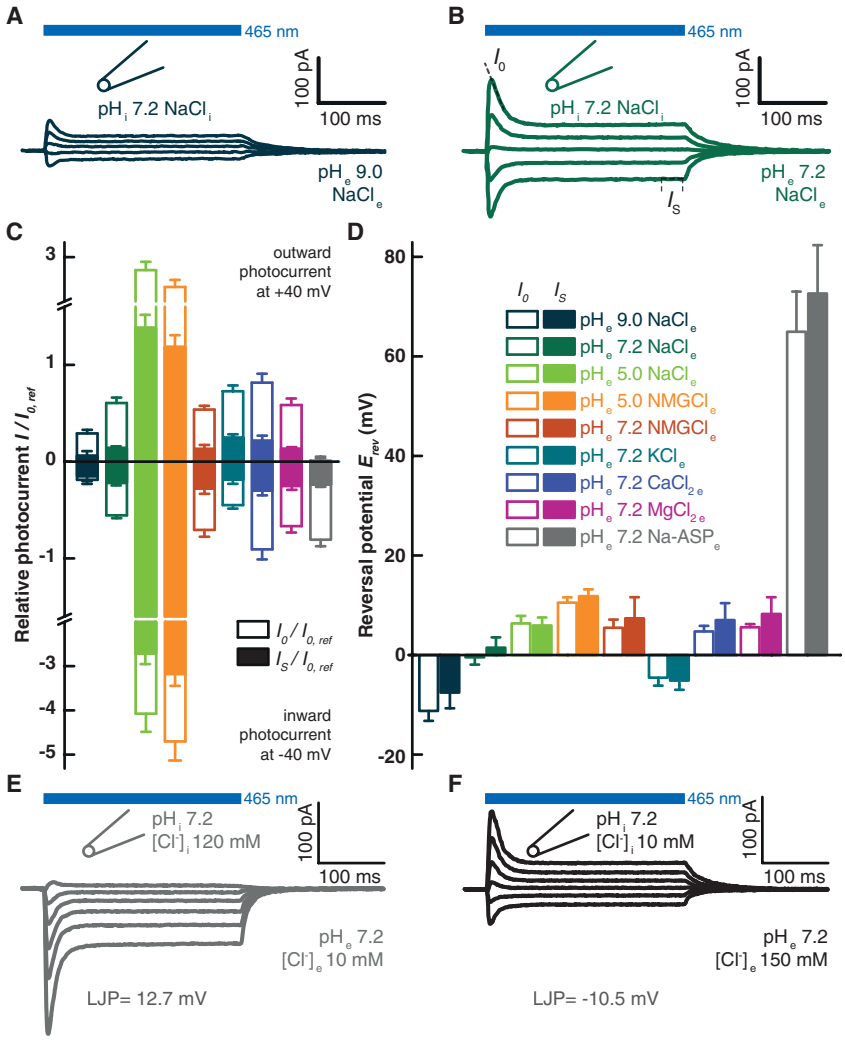

Fig. 2. Ion selectivity of C2-EK-TC. (**A** and **B**) Representative photocurrent traces of C2-EK-TC recorded in HEK293 cells. The internal solution was maintained at high NaCl, pH$_i$ 7.2, whereas the external solution varied as indicated. Voltage was clamped from −40 mV to +40 mV in 20-mV steps. The initial photocurrent (I_0) is determined by linear extrapolation to $I_{(t=0)}$. (**C**) Comparison of initial current amplitudes at −40 mV and +40 mV for different external cations. Photocurrents were normalized to the initial photocurrent at reference conditions (I_0, ref: high NaCle, pHe 7.2, −60 mV) (**D**) Corresponding reversal voltage (E_{rev}) for all conditions. (D and E) Light-gray bars reflect conditions of reduced external Cl^-. (**E** and **F**) Photocurrent traces of C2-EK-TC recorded in HEK293 cells. Voltage was clamped from −60 mV to +40 mV in 20-mV steps in addition to the present liquid junction potential (LJP), as indicated. (E) The internal solution contained high Cl^- (120 mM), and the external solution contained a reduced Cl^- concentration (10 mM). (F) Inverse Cl^- conditions of 10 mM (internal) and 150 mM (external). Mean values ± SEM ($n \geq 6$ HEK293 cells) are illustrated.

type (Fig. 1A), indicating that the protein interior is not accessible for chloride. The Cl^- distribution of the E90K and E90R mutants as shown in Fig. 1, B and C, which denote a region where the free energy is lower than that in bulk phase, is now continuous from the extracellular side to the active site. On the other hand, K^+ free energy decreases by 25% in E90K and 40% in E90R at the maximum point (table S2). The differences in the dark-state Cl^- distributions of E90K and E90R mutants may result from differences in shape and electrostatic interaction in the cavity next to K and R. Taken together, our data demonstrate that increased Cl^- affinity, higher protein flexibility, and a larger cavity induced by disruption of the hydrogen-bonded network may all contribute to the high Cl^- conductance and selectivity of E90K and E90R.

Encouraged by the favorable properties of the engineered chloride channel, we tested its potential application in neuroscience. In the brain, ligand-gated Cl^- channels [such as γ-aminobutyric acid type A ($GABA_A$) receptors] mediate fast inhibition of neural activity by shunting depolarizing currents. Efficient mechanisms for Cl^- removal keep the internal Cl^- concentration low in mature neurons, providing a steep concentration gradient across the plasma membrane (*31*). On the basis of this, we hypothesized that ChloCs could be used as a tool to provide light-induced inhibition of neuronal spiking. To test this concept, we transfected CA1 pyramidal cells in organotypic hippocampal culture, with a bicistronic plasmid coding for slow ChloC and a red fluorescent protein (tdimer2). Two-photon imaging of transfected neurons revealed normal spine densities on oblique dendrites (Fig. 4A and fig. S8). Passive and active membrane properties did not differ from neurons expressing the previously characterized and well-tolerated ChR2-E123T-T159C mutant (*25*) or nontransfected neurons (table S4).

To determine the E_{rev} of slow ChloC, we performed voltage-clamp recordings in CA1 pyramidal cells. Photocurrents were large and outlasted the 2-ms light pulse by many seconds (τ_{off} = 10.5 ± 0.3 s) (Fig. 4B). Current direction reversed at –68.2 ± 0.8 mV (n = 6 neurons)—more negative than ChloC (–61.8 ± 1.0 mV, n = 6 neurons), E90K-T159C (–42.9 ± 1.7 mV, n = 6 neurons), and E123T-T159C (–3.2 ± 2.0 mV, n = 5 neurons), which is consistent with the high Cl^- conductance of E90R mutants observed in HEK293 cells (Fig. 3 and fig. S5). Next, we tested the effects of slow ChloC activation on AP generation. Depolarizing somatic current injections evoked a reproducible train of 5 to 6 APs in transfected neurons. Activation of slow ChloC by a 5-ms light pulse completely blocked AP generation (Fig. 4E), whereas ChloC could be used to block spikes in a more defined time window with millisecond precision (Fig. 4F). Activation of ChloCs was accompanied by a small depolarization, reflecting the difference between the very negative resting voltage of CA1 pyramidal cells (–77 mV) (table S4) and the E_{rev} of ChloC. Thus, unlike previously published light-driven ion pumps [such as halorhodopsin or archaerhodopsin (Arch)], ChloCs do not provide inhibition by hyperpolarization but shunt excitatory currents very efficiently.

Next, we sought to determine whether ChloC could also prevent APs triggered by strong synaptic input. Stimulating afferent fibers with an extracellular electrode placed in stratum radiatum evoked single APs. Pairing synaptic stimulation with brief pulses of blue light inhibited ~90% of evoked APs in ChloC-expressing neurons, whereas slow ChloC achieved 100% block (fig. S10). How do the light sensitivities of ChloC and slow ChloC compare with the light-driven proton pump Arch (*8*)? To determine the minimal current necessary to evoke a spike (rheobase), we injected depolarizing current ramps into CA1 pyramidal neurons. In the dark, both transfected and nontransfected neurons had similar rheobases between 150 and 200 pA (table S4). At high light intensities (10 mW/mm^2), Arch strongly hyperpolarized neurons and shifted the rheobase by 280 pA. To produce a similar shift in rheobase, cells expressing slow ChloC needed ~10,000 times less light (Fig. 4, G and H). At light intensities of 0.1 mW/mm^2 and above, slow ChloC-expressing neurons could not be driven to spike anymore. Because fast Na^+ channels tend to inactivate during depolarizing ramps, we also applied voltage step protocols to measure spike output at various light levels, confirming the very high sensitivity of slow ChloC (fig. S11).

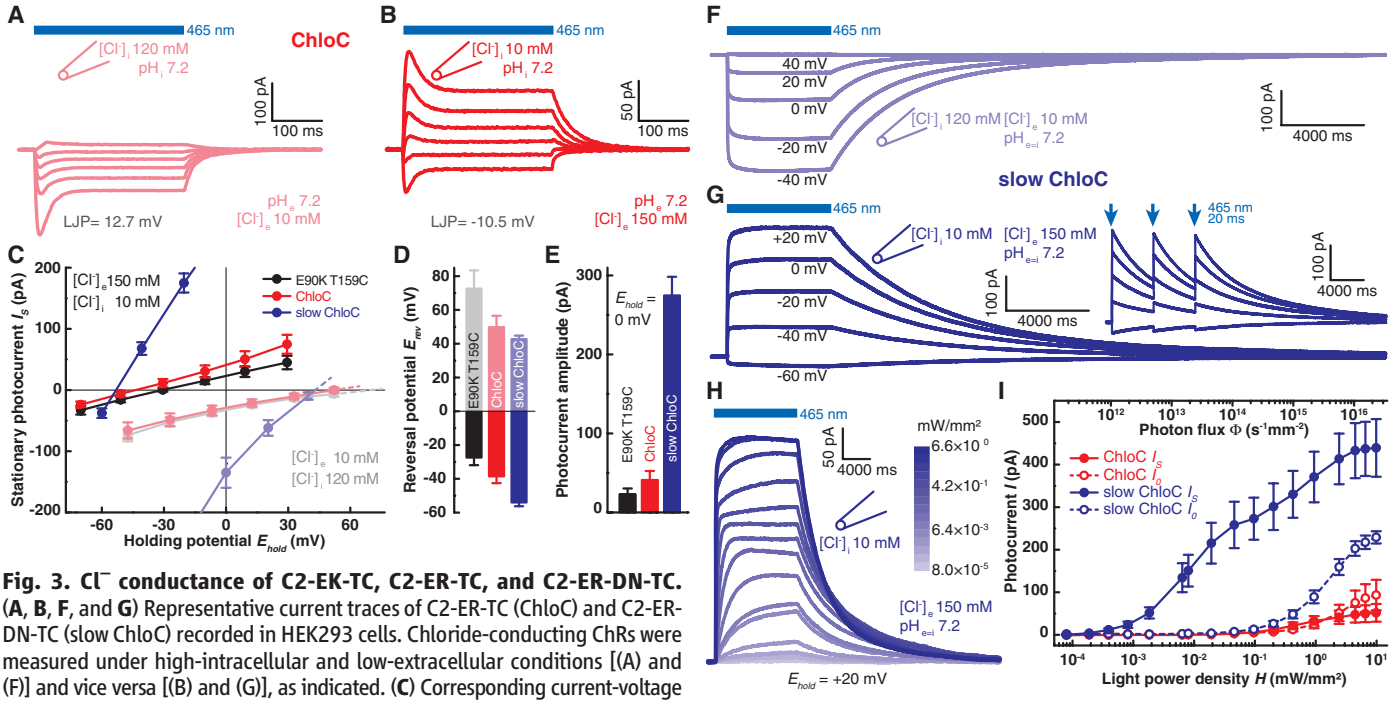

Fig. 3. Cl^- conductance of C2-EK-TC, C2-ER-TC, and C2-ER-DN-TC. (**A**, **B**, **F**, and **G**) Representative current traces of C2-ER-TC (ChloC) and C2-ER-DN-TC (slow ChloC) recorded in HEK293 cells. Chloride-conducting ChRs were measured under high-intracellular and low-extracellular conditions [(A) and (F)] and vice versa [(B) and (G)], as indicated. (**C**) Corresponding current-voltage relationships in comparison with C2-EK-TC. (**D**) Reversal potentials (E_{rev}) for C2-EK-TC, ChloC, and slow ChloC at high-intracellular and low-extracellular conditions (top light bars) and vice versa (bottom dark bars) as same conditions as in (C). (**E**) Comparison of photocurrent amplitudes for different chloride-conducting C2 variants at 0 mV holding potential. (**H**) Photocurrents of slow ChloC at different light intensities. (**I**) Amplitudes of the initial current I_0 (20-ms flash) and stationary current I_S of ChloC (300-ms light pulse) and slow ChloC (12 s illumination) at different light intensities. Mean values ± SEM ($n \geq 6$ HEK293 cells) are illustrated.

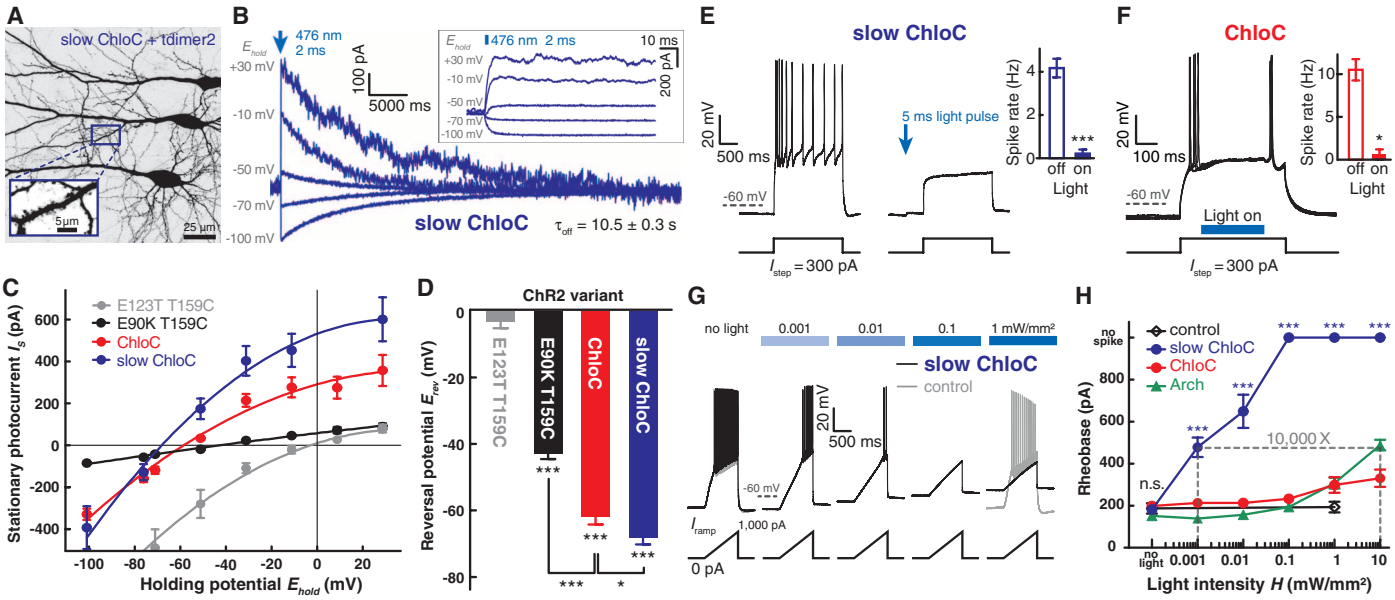

Fig. 4. Characterization of ChloC variants in CA1 pyramidal neurons. (**A**) CA1 pyramidal neurons expressing slow ChloC (C2-ER-DN-TC) and cytosolic tdimer2. Contrast-inverted maximum intensity projection. (**B**) Light-evoked (1 mW/mm^2) photocurrents in a slow ChloC-expressing pyramidal cell at different holding potentials (junction-potential corrected). (Inset) First 100 ms after light pulse. (**C**) *I*/*E* relation of stationary photocurrents. (**D**) Reversal potential measurements of photocurrents [one-way analysis of variance (ANOVA), Tukey's test, $P < 0.001$]. (**E**) Somatic current injections (2 s, 300 pA) induced AP firing in slow ChloC-expressing neurons in the dark with typical accomodation. A brief light pulse (5 ms, 476 nm, 1 mW/mm^2) 100 ms before the current step blocked AP firing (paired *t* test, $P < 0.001$, $n = 7$ neurons). (**F**) Light activation (300 ms) during somatic current injections (500 ms, 300 pA) blocked AP firing in ChloC-expressing neurons ($P = 0.01$, $n = 4$ neurons). (**G**) In slow ChloC-expressing neurons, blue light at increasing intensities (1 µW/mm^2 to 1 mW/mm^2) gradually raised the rheobase of current-ramp–evoked APs (black traces). There was no effect of blue light in wild-type cells (gray traces). (**H**) Comparison of rheobase at different light intensities between wild-type neurons (control) and neurons expressing ChloC, slow ChloC, or Arch. Rheobase was similar in all cells in the dark ($P = 0.2$). ANOVA, ***$P < 0.001$; n.s., not significant.

Thus, ChloCs mimic the effect of physiological inhibition through $GABA_A$ receptor activation. Photocurrents showed only little inactivation during long light pulses (fig. S9), and optical neuronal inhibition was fully reversible (fig. S12).

Because only one single charge is transported per photocycle, inhibitory ion pumps must be continuously activated with intense light to maintain high turnover and inhibition. In contrast, single-photon absorption of a light-gated chloride channel enables continuous chloride flux until the respective channel closes by means of thermal relaxation. Slow ChloC should be advantageous for in vivo applications because a very large volume of brain tissue could be addressed by a single optical fiber or head-mounted light-emitting diode. For applications requiring temporally precise inhibition in the blue spectrum, ChloC is a viable alternative to Arch or halorhodopsin, and ChloCs with intermediate kinetics could be generated on demand. We hope that blocking the output of identified neurons will enable investigators to assess the contribution of specific neuronal populations to learning, memory, and other brain functions in a fully reversible fashion.

References and Notes

1. G. Nagel *et al.*, *Science* **296**, 2395–2398 (2002).
2. G. Nagel *et al.*, *Proc. Natl. Acad. Sci. U.S.A.* **100**, 13940–13945 (2003).
3. O. A. Sineshchekov, K. H. Jung, J. L. Spudich, *Proc. Natl. Acad. Sci. U.S.A.* **99**, 8689–8694 (2002).
4. O. Yizhar, L. E. Fenno, T. J. Davidson, M. Mogri, K. Deisseroth, *Neuron* **71**, 9–34 (2011).
5. F. Zhang *et al.*, *Cell* **147**, 1446–1457 (2011).
6. X. Han, E. S. Boyden, *PLOS ONE* **2**, e299 (2007).
7. F. Zhang *et al.*, *Nature* **446**, 633–639 (2007).
8. B. Y. Chow *et al.*, *Nature* **463**, 98–102 (2010).
9. H. E. Kato *et al.*, *Nature* **482**, 369–374 (2012).
10. A. P. Plazzo *et al.*, *J. Biol. Chem.* **287**, 4818–4825 (2012).
11. Y. Sugiyama *et al.*, *Photochem. Photobiol. Sci.* **8**, 328–336 (2009).
12. K. Ruffert *et al.*, *Biochem. Biophys. Res. Commun.* **410**, 737–743 (2011).
13. D. Gradmann, A. Berndt, F. Schneider, P. Hegemann, *Biophys. J.* **101**, 1057–1068 (2011).
14. H. C. Watanabe *et al.*, *J. Biol. Chem.* **287**, 7456–7466 (2012).
15. Single-letter abbreviations for the amino acid residues are as follows: A, Ala; C, Cys; D, Asp; E, Glu; F, Phe; G, Gly; H, His; I, Ile; K, Lys; L, Leu; M, Met; N, Asn; P, Pro; Q, Gln; R, Arg; S, Ser; T, Thr; V, Val; W, Trp; and Y, Tyr. In the mutants, other amino acids were substituted at certain locations; for example, E90K indicates that glutamic acid at position 90 was replaced by lysine.
16. K. Eisenhauer *et al.*, *J. Biol. Chem.* **287**, 6904–6911 (2012).
17. V. A. Lórenz-Fonfría *et al.*, *Proc. Natl. Acad. Sci. U.S.A.* **110**, E1273–E1281 (2013).
18. H. C. Watanabe, K. Welke, D. J. Sindhikara, P. Hegemann, M. Elstner, *J. Mol. Biol.* **425**, 1795–1814 (2013).
19. L. A. Gunaydin *et al.*, *Nat. Neurosci.* **13**, 387–392 (2010).
20. S. Ito *et al.*, *J. Am. Chem. Soc.* **136**, 3475–3482 (2014).
21. H. Watanabe, M. Elstner, T. Steinbrecher, *J. Comput. Chem.* **34**, 198–205 (2013).
22. D. Beglov, B. Roux, *J. Phys. Chem. B* **101**, 7821–7826 (1997).
23. A. Kovalenko, F. Hirata, *J. Chem. Phys.* **110**, 10095 (1999).
24. E. Ritter, K. Stehfest, A. Berndt, P. Hegemann, F. J. Bartl, *J. Biol. Chem.* **283**, 35033–35041 (2008).
25. A. Berndt *et al.*, *Proc. Natl. Acad. Sci. U.S.A.* **108**, 7595–7600 (2011).
26. S. Ullrich, R. Gueta, G. Nagel, *Biol. Chem.* **394**, 271–280 (2013).
27. A. Berndt, M. Prigge, D. Gradmann, P. Hegemann, *Biophys. J.* **98**, 753–761 (2010).
28. K. Nikolic *et al.*, *Photochem. Photobiol.* **85**, 400–411 (2009).
29. N. Grossman, K. Nikolic, C. Toumazou, P. Degenaar, *IEEE Trans. Biomed. Eng.* **58**, 1742–1751 (2011).
30. F. Schneider, D. Gradmann, P. Hegemann, *Biophys. J.* **105**, 91–100 (2013).
31. C. Rivera *et al.*, *Nature* **397**, 251–255 (1999).

Acknowledgments: We thank M. Reh, A. Klein and I. Ohmert for excellent technical support and R. Schwarzer and A. Herrmann for assistance with confocal microscopy. This work was supported by the Leibniz Graduate school (A.V.) and the Deutsche Forschungsgemeinschaft (SFB1078, B2 to P.H., FOR1279 to M.E. and P.H., and SPP1665 to P.H. and T.G.O.).

Supplementary Materials

www.sciencemag.org/content/344/6182/409/suppl/DC1
Materials and Methods
Figs. S1 to S12
Tables S1 to S4
References

5 December 2013; accepted 13 March 2014
Published online 27 March 2014;
10.1126/science.1249375